Dynamic analysis of non-smooth contact in bladed disk root joints via an equality-based frequency domain method

Sebastian Mcdonald, Mathias Legrand, Christophe Pierre

17th International Symposium on Unsteady Aerodynamics
Aeroacoustics and Aeroelasticity of Turbomachines
ISUAAAT17
November 16-21, 2025, Melbourne, Australia

ISUAAAT17-67

DYNAMIC ANALYSIS OF NON-SMOOTH CONTACT IN BLADED DISK ROOT JOINTS VIA AN EQUALITY-BASED FREQUENCY DOMAIN METHOD

Sebastian McDonald & Mathias Legrand
Department of Mechanical Engineering, McGill University
Christophe Pierre
Department of Mechanical Engineering, Stevens Institute of Technology

Corresponding Author: ***Sebastian McDonald***
sebastian.mcdonald@mail.mcgill.ca

KEY WORDS

Bladed disk vibrations, Non-smooth dynamics, Friction, Unilateral contact, Wear, Harmonic balance method

ABSTRACT

A novel frequency-domain framework for modeling fretting wear under oscillatory contact is presented, unifying friction, separation, and wear within a single formulation. The classical Signorini and Coulomb conditions are recast as non-smooth, equality-based expressions that augment the equations of motion, all of which are efficiently solved using the harmonic balance method. Wear evolution is modeled via a dual time scale approach with Archard's law. Further integrated within a finite element framework, the method is demonstrated on a bladed disk model subject to root contact and harmonic tip excitation. Extended studies demonstrate the preservation of the non-smooth contact sets for reasonable harmonic truncation orders and predict classical friction-dampening effects. Elevated surface degradation in critically loaded regions is also observed. Ultimately, these developments enable a detailed investigation of the complex interplay among stick-slip, separation, and wear progression, providing a robust tool for analyzing frictional contact and wear in turbomachinery applications.

BACKGROUND AND INTRODUCTION

Accurate and efficient modeling of frictional contact is essential in modern turbomachinery structural dynamics. Classically, non-smooth impenetrability and friction laws describe these interactions. Various methods have emerged to predict blade vibrations in the presence of contact, notably combinations of penalty- and Lagrangian-based methods [1]. In the time domain, these approaches are realized alongside dedicated time integration strategies [2]. Alternatively, accelerative weighted residual techniques, such as the widely used harmonic balance method, solve these conditions in a weak sense. Because of their non-smooth nature, frictional contact conditions cannot be expressed in a closed form and must employ alternating frequency/time (AFT) procedures. AFT schemes iteratively calculate the contact forces in the time-domain from frequency-domain displacements and velocities, until convergence is achieved. The most effective AFT-based strategy is the Dynamic-Lagrangian Frequency Time (DLFT) method [3]. DLFT has seen notable success in modeling aeroengine frictional contact in increasingly advanced contexts; however, its solution strategy is complex and difficult to implement, which may lead to computational inefficiencies and integration challenges.

Modeling surface wear and its effects on turbomachinery dynamics remains an ongoing challenge, due in particular to the limitations of existing strategies in capturing repeated contact interactions over large numbers of loading cycles. While time-domain approaches offer high-fidelity algorithms for non-smooth contact, they require a fine discretization, which for rapid vibrations can become prohibitively expensive. Conversely, alternative weighted residual techniques are more efficient but often impose simplified contact conditions, such as regularization, or incorporate complex solution strategies as in the case of DLFT. Material removal that occurs as a natural result

of impact and friction interactions further complicates the long-term prediction of system behavior, since the geometry and contact conditions evolve over repeated loading cycles. Numerically, wear laws parameterize the rate at which surfaces evolve. Under the small-sliding assumption, Archard's wear law [4], which defines wear as proportional to the product of normal contact force and sliding distance, is typically used. Coupled dynamic–wear analyses of aeroengine root contact in a weighted residual framework were notably carried out by Salles [5] and Lemoine [6]. Their results highlight intricate contact-wear effects, which are further examined in the present work.

The developments presented in this paper address the aforementioned limitations. Specifically, a novel Equality-based Weighted Residual (E-WR) formulation, recently developed for periodic solutions of systems with frictional occurrences [7], is generalized to the case of impenetrability and friction at multiple contact points. The formulation is further integrated within a finite element framework and applied to analyze friction and impenetrability in the root attachment of a bladed disk structure subject to fretting.

FRICTIONAL CONTACT MODEL

The governing equations of elasticity define the equilibrium conditions for the strain response of deformable bodies. In this context, the balance of linear momentum is enforced at the contact interface. Impenetrability and frictional interactions are described by the conditions of Signorini and Coulomb, respectively. Following an appropriate finite element spatial discretization and component mode synthesis, the fundamental equations can be written as

$$\mathbf{M}\ddot{\mathbf{q}} + \mathbf{D}\dot{\mathbf{q}} + \mathbf{K}\mathbf{q} - \mathbf{L}\boldsymbol{\lambda} - \mathbf{f} = \mathbf{0} \tag{1}$$

$$\lambda_{T_k} - \text{proj}_{(C)}(\lambda_{T_k} - \rho_{T_k}\dot{\mathrm{q}}_{T_k}) = 0 \tag{2}$$

$$\lambda_{N_k} - \text{proj}_{(C)}(\lambda_{N_k} - \rho_{N_k}(\mathrm{q}_{N_k} + g_{0_k})) = 0 \tag{3}$$

$$\rho_{T_k} > 0, \qquad \rho_{N_k} > 0, \qquad k = 1, \cdots, K_c$$

where Equation (1) expresses the governing equations of elasticity in terms of the generalized coordinate vector $\mathbf{q}$, the mass, damping, and stiffness matrices $\mathbf{M}$, $\mathbf{D}$, and $\mathbf{K}$, the external forcing vector $\mathbf{f}$, and the frictional contact load vector $\boldsymbol{\lambda} \equiv (\boldsymbol{\lambda}_N, \boldsymbol{\lambda}_T)$, where the subscripts N and T refer to the normal and tangential components of the mechanical degrees of freedom at the contact interface. The location matrix $\mathbf{L}$ maps the nonlinear contact forces $\boldsymbol{\lambda}$ onto the appropriate entries in the global force vector, that is, aligned with the organization of the generalized coordinates.

Equations 2 and 3 present proximal, equality-based representations of the Coulomb and Signorini conditions, respectively, for k in K_c total contact points. Henceforth, the contact point subscript is omitted for readability. Within this framework C defines the contact sets for variable normal forcing with separation – that is the *true* friction cone.

For impenetrability, orthogonality is enforced between the sum of the normal displacement q_N and the gap function g_0 with the normal contact force λ_N. Similarly, for friction, a corresponding relation is imposed between the tangential velocity $\dot{\mathrm{q}}_T$ and the in-plane contact load λ_T. This relation further prescribes $|\lambda_T| = \mu\lambda_N \quad$ when $\dot{\mathrm{q}}_T \neq 0$, where μ is the coefficient of friction. Mathematically, the friction (Ψ_c) and impenetrability (Ψ_s) sets therefore impose

$$\Psi_c = \begin{cases} \dot{\mathrm{q}}_T = 0 \Rightarrow & |\lambda_T| \leq \mu\lambda_N \\ \dot{\mathrm{q}}_T \neq 0 \Rightarrow & |\lambda_T| = \mu\lambda_N \end{cases} \tag{4}$$

$$\Psi_s = \begin{cases} \mathrm{q}_n = g_0 \Rightarrow & \lambda_N \geq 0 \\ \mathrm{q}_n > g_0 \Rightarrow & \lambda_N = 0 \end{cases} \tag{5}$$

Figure 1 depicts these relations graphically for a section of the friction cone. The solution sets for Equations 2 and 3 are preserved in the level-set form of Equations 4 and 5. It is noted here that there is an imposition on the direction of the normal contact force. In this respect, λ_N is explicitly non-negative with positive displacements characterizing separation. Furthermore, λ_T and λ_N are not necessarily constant during sliding as they are depicted graphically. To this end, they evolve along the peripheral surface (with respect to the normal axis) of the friction cone.

The method used to find the periodic solutions of the frictional contact problem subject to a periodic external forcing follows the E-WR strategy developed in [7]. In this approach, the contact conditions in Equation 2 and 3 are recast as equivalent non-smooth expressions.

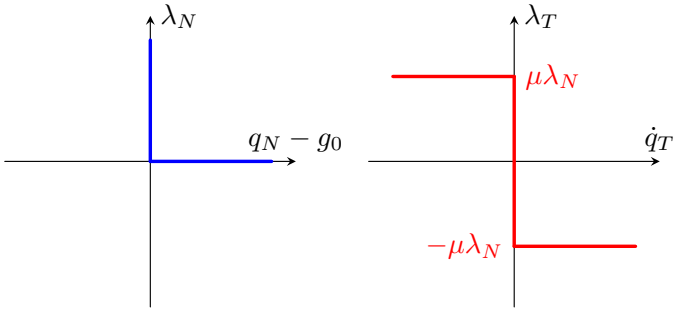

FIGURE 1. Signorini (left) and Coulomb (right) solution sets

For one-dimensional friction, as is explored in this work, the expression is explicitly that of the original reference

$$\Psi_c = \dot{\mathrm{q}}_T + \min\left(0, \rho_T(\lambda_T + \mu\lambda_N) - \dot{\mathrm{q}}_T\right) + \max\left(0, \rho_T(\lambda_T - \mu\lambda_N) - \dot{\mathrm{q}}_T\right) \quad (6)$$

which, for the various cases of the min and max functions, can be expressed in piecewise form as

$$\Psi_c = \begin{cases} \rho_T(\lambda_T - \mu\lambda_N) & \text{if } \rho_T(\lambda_T + \mu\lambda_N) - \dot{\mathrm{q}}_T > 0 \\ & \quad \text{and } \rho_T(\lambda_T - \mu\lambda_N) - \dot{\mathrm{q}}_T > 0, \\ \dot{\mathrm{q}}_T & \text{if } \rho_T(\lambda_T + \mu\lambda_N) - \dot{\mathrm{q}}_T > 0 \\ & \quad \text{and } \rho_T(\lambda_T - \mu\lambda_N) - \dot{\mathrm{q}}_T < 0, \\ \rho_T(\lambda_T + \mu\lambda_N) & \text{if } \rho_T(\lambda_T + \mu\lambda_N) - \dot{\mathrm{q}}_T < 0 \\ & \quad \text{and } \rho_T(\lambda_T - \mu\lambda_N) - \dot{\mathrm{q}}_T < 0 \end{cases} \quad (7)$$

Conversely, for impenetrability, the expression is derived from the theorems presented in [8]

$$\Psi_s = \lambda_N + \min\left(0, \rho_N(\mathrm{q}_N - g_0) - \lambda_N\right) \quad (8)$$

which can be expanded as

$$\Psi_s = \begin{cases} \lambda_N & \text{if } \rho_N(\mathrm{q}_N - g_0) - \lambda_N > 0 \\ \rho_N(\mathrm{q}_N - g_0) & \text{if } \rho_N(\mathrm{q}_N - g_0) - \lambda_N < 0 \end{cases} \quad (9)$$

Collectively, Ψ_c and Ψ_s describe non-smooth line contact. Here, friction-impenetrability coupling is demonstrated in the dependency of Ψ_c on λ_N. For reference an uncoupled equality-based formulation of planar friction for a singular contact point can be found in [9].

EQUALITY BASED WEIGHTED RESIDUAL METHOD

The equality-based contact laws in Equations 6 and 8 are resolved for each contact point k. Alongside the governing equation of elasticity they are treated in a weak sense via the harmonic balance method. Thus, the modified contact problem for one-dimensional friction reads

$$\forall m, \quad \int_0^T \phi_m(t)\left(\mathbf{M}\ddot{\mathbf{q}} + \mathbf{D}\dot{\mathbf{q}} + \mathbf{K}\mathbf{q} - \mathbf{L}\boldsymbol{\lambda} - \mathbf{f}\right) \mathrm{d}t = \mathbf{0} \quad (10)$$

$$\forall m, \quad \int_0^T \phi_m(t)\left(\lambda_N + \min\left(0, \rho_N(\mathrm{q}_N - g_0) - \lambda_N\right)\right) \mathrm{d}t = 0 \quad (11)$$

$$\forall m, \quad \int_0^T \phi_m(t)\Big(\dot{\mathrm{q}}_T + \min\left(0, \rho_T(\lambda_T + \mu\lambda_N) - \dot{\mathrm{q}}_T\right) + \max\left(0, \rho_T(\lambda_T - \mu\lambda_N) - \dot{\mathrm{q}}_T\right)\Big) \mathrm{d}t = 0 \quad (12)$$

where $\phi_m(t)$, for $m = -N_\phi, \cdots, N_\phi$, are the Fourier basis functions with which the generalized coordinates and contact forces are approximated by and projected upon, over the period of interest T. Explicitly, one has

$$\mathbf{q}(t) \approx \mathbf{q}_h(t) = \sum_{m=-N_\phi}^{N_\phi} \mathbf{q}_m \phi_m(t), \quad (13)$$

$$\boldsymbol{\lambda}(t) \approx \boldsymbol{\lambda}_h(t) = \sum_{m=-N_\phi}^{N_\phi} \boldsymbol{\lambda}_m \phi_m(t) \quad (14)$$

with $\phi_m(t) = e^{\frac{im}{T}t}$ indicating the inclusion of all odd-, even- and zeroth-order harmonics for a truncation order of N_ϕ. Here, the inclusion of the zeroth-harmonic is understood to recover non-unique frictional forcing in sticking instances, as is explored in [10]. To remedy this, all static contributions to λ_T are nullified. Furthermore, it should be noted that the omission of a spatial integral in the modified contact conditions is intentional, as Dirac shape functions are employed in a node-to-node discretization of the contact interface. Following substitution of Equations 13 and 14 into Equations 10 – 12 the contact problem is posed as a function of harmonic coefficients $\boldsymbol{\lambda}_m$ and $\mathbf{q}_m$.

DYNAMIC CONDENSATION

Considering K_s as the number of generalized coordinates, the resulting system of equations is of size $(2N_\phi + 1) \times (K_s + 2K_c)$. In this E-WR based method, the linearity of Equation 10 in $\mathbf{q}$ is leveraged to reduce the order of this system and remove its dependence on K_s through a process known as dynamic condensation. In this procedure, the displacement harmonics $\hat{\mathbf{q}} = [\mathbf{q}_0, \mathbf{q}_1, ..., \mathbf{q}_m]$ are recast as explicit functions of the nonlinear force harmonics. Hence,

$$\hat{\mathbf{q}} = \left(\hat{\nabla}^2 \otimes \mathbf{M} + \hat{\nabla}^1 \otimes T\mathbf{D} + \hat{\nabla}^0 \otimes T^2\mathbf{K}\right)^{-1}\left(\hat{\nabla}^0 \otimes T^2\mathbf{I}\right)\left(\hat{\mathbf{L}}\hat{\lambda} + \hat{\mathbf{f}}\right) \quad (15)$$

where $\hat{\nabla}$ denotes the time-derivative matrix and $\hat{L}$ the location matrix, both defined in the frequency domain. Inherently, Equation 15 is the transformation associated with the orthogonal projection of $\phi_m(t)$ on linear inertial force terms in governing equation of elasticity.

Ultimately, Equation 15 enables the contact problem to be solved with residual equations 11 and 12 exclusively as a sole function of $\hat{\boldsymbol{\lambda}}$, or otherwise, $\boldsymbol{\lambda}_m$ for $m = -N_\phi, \cdots, N_\phi$ at each contact point, $k \in K_c$, as it is presented in the contact conditions. This represents a system of nonlinear and necessarily non-smooth algebraic equations of size $(2N_\phi + 1) \times (2K_c)$. The solution strategy hence follows a Newton-Raphson procedure wherein iterative transformation from the nonlinear force to displacement harmonics are carried out in minimizing these residual functions.

WEAR MODELING

The effects of surface wear are realized in the form of an evolving gap function. Within a finite element context, this is modeled as increasing permanent separation between the individual nodes of the discretized surfaces. The evolution of the magnitude of separation, captured by g_0, with respect to time is defined according to the prescribed wear law. For significantly damaging contact, wear influences the dynamic response over individual loading cycles, necessitating its discretization as an additional set of unknowns. Conversely, in less intense regimes as is the case of fretting wear, the amount of wear may be considered constant over individual loading cycles. This notion justifies the use of two time scales: a fast one associated with the dynamics of the contact problem, imposing a constant gap function, and a slow one describing the progression of wear.

The use of two time scales in this manner was originally proposed by Salles [5] and is incorporated in this approach. In the context of weighted residual methodologies, the method reduces the generalized dynamic-wear problem into the resolution of a series of consecutive contact problems. The incurred wear in this strategy is computed using Archard's wear law at each vibration cycle, n, over a total of N_w cycles, according to

$$g_0^{N_w} = \sum_{n=0}^{N_w} g_0^n, \qquad \text{with} \qquad g_0^{n+1} = \int_0^T k_w |\lambda_N^n| |\dot{\mathrm{q}}_T^n| \, \mathrm{d}t \quad (16)$$

herein the superscript references the proceeding load cycle that wear propagates upon that is separate from that of the dynamics, t.

INDUSTRY CASE STUDY

The frictional contact and wear methodologies described above are applied to a bladed-disk model provided by Safran Helicopter Engines. The geometry, shown in Figure 2, consists of a single blade and its corresponding disk sector, connected at the blade's fir-tree root. For the simplified 2D model considered here, both the blade and disk are made of a titanium alloy. The model is discretized using a quadrilateral-dominant mesh with approximately 2100 nodes. Moreover, the

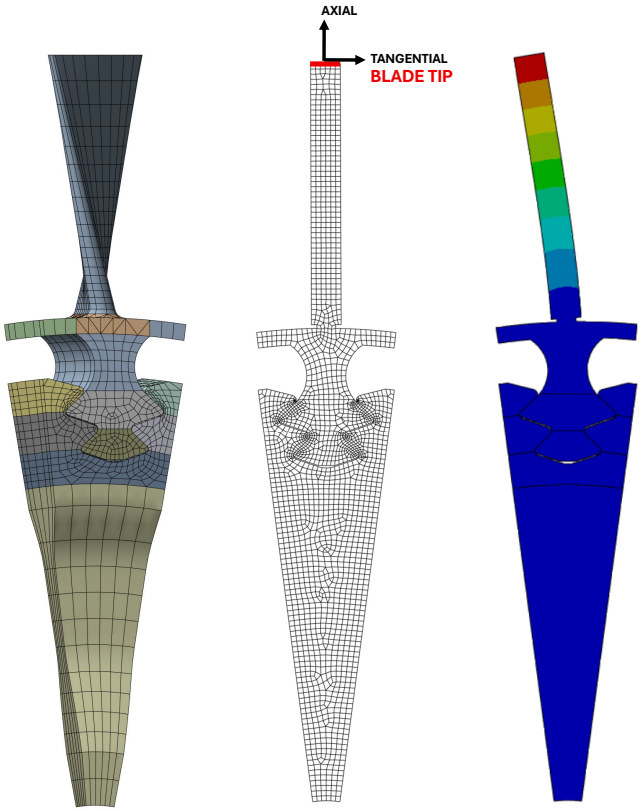

FIGURE 2. Finite element models of a bladed disk sector with fir-tree attachment: full 3D (left) and simplified 2D (middle) geometries with first full-stick mode shape (right)

contact interface comprises 40 equally spaced contact pairs across the four engaged surfaces at the root attachment, as shown in Figure 3. Each of these contact pairings imposes impenetrability in the normal direction (N) and friction in the tangential direction (T). Furthermore, plane stress conditions are imposed, with the bladed disk being treated as fully clamped with free-free boundary conditions on the blade. To establish the point of static

equilibrium, the rigid body modes of the blade are eliminated following the approach in [11]. The bladed disk model is therefore analyzed with respect to the unloaded reference configuration, in which the blade and disk root interfaces are coincident.

Periodic responses of the coupled structure are studied in the frequency range of the first full-stick mode mode of vibration at 1090 Hz, under harmonic excitation conditions that induce sliding amplitudes in the range of fretting wear. The applied forces enforce a static axial load and a dynamic tangential load at the blade tip, highlighted in Figure 2. The axial load emulates centrifugal effects and the dynamic load captures aeroelastic excitations at the operational conditions of the aeroengine. In these studies, the coefficient of friction and the excitation frequency are varied under the assumption that there is no initial separation at the attachment interface.

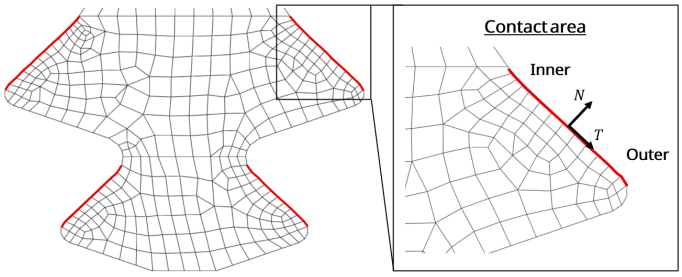

FIGURE 3. Contact regions (▬) of the blade at the blade-disk root joint

CONTACT MODEL VALIDATION

The E-WR formulation is first validated to establish its accuracy in preserving the impenetrability and friction sets for the model considered. Herein, wear effects are omitted. These studies impose a friction coefficient of 0.2 and explore quasi-static and dynamic loading effects at 500 Hz. In these investigations $N_\phi = 15$ and 2^{10} discrete time samples are used in the weighted residual procedure.

The results presented in Figure 4 compare the solution sets of the truly non-smooth contact conditions with those obtained using the E-WR method, at one of the top contact interfaces. These results are broadly representative of all individual surfaces. Overall, the method demonstrates strong agreement with the true contact sets. Minute differences are attributed to the Gibbs phenomenon that arises as a natural result of the weighted-residual nature of the method. It should be noted that showing only part of the friction cone can misrepresent the method's satisfaction of the Coulomb condition, since the reference set assumes a constant normal force. This limitation is, however, partially mitigated by the quasi-static nature of the analysis. Further evident in this figure is the distribution of separation, sliding velocities and contact pressures in the contact interface. These results reveal that the natural geometry of the bladed-disk system causes the root interface to exhibit greater separation near its outer edge. Toward the central, innermost region, contact pressures and slip velocities increase, although slip remains largely uniform.

The effects of dynamic loading on the normal contact forces in the blade–root interface are depicted in Figure 5. These plots present the maximum normal forces across the span of the top two contact interfaces and reveal a symmetry in the force distribution. Moreover, the previously quasi-static pressure profile becomes increasingly curved, with elevated magnitudes particularly near the periphery of the contact zone. Deviations from this trend can be attributed to both asymmetric tip-root coupling and frictional effects. Phenomenologically, this behavior arises from the

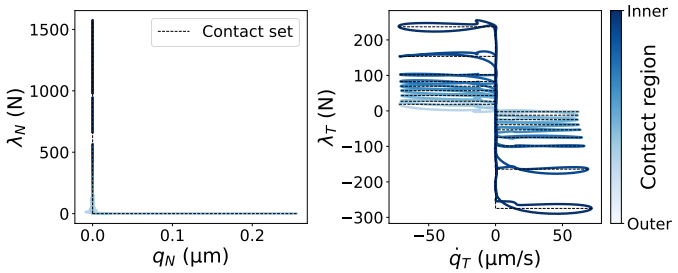

FIGURE 4. E-WR impenetrability (left) and friction (right) solution sets of the top left-left most root interface

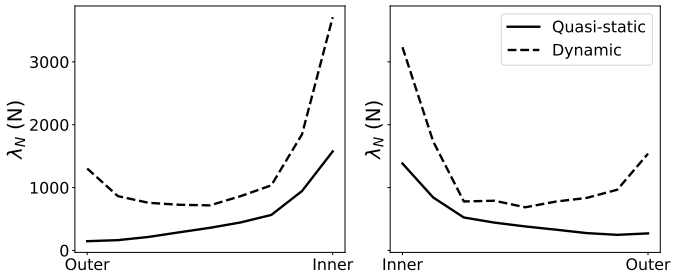

FIGURE 5. Normal contact force distribution of the top contact interfaces

oscillatory motion of the blade, which causes the interfaces to slip and pivot about the central region. In regimes characterized by largely homogeneous sliding velocities, it will be shown that this effect most critically governs the distribution of surface wear.

FRICTION DAMPING

The effects of increased friction are examined in the absence of wear for a harmonic truncation order of $N_\phi = 5$. This value is used for all subsequent analyses and was configured based on the convergence properties of the contact force and wear distributions at the root interface. Similar harmonic orders have been employed in related works [5]. Consistent with the role of contact interactions at the root interface in enhancing structural damping, these studies focus on quantifying variations in the dynamic response at the blade tip as influenced by blade root stick–slip and separation. To this end, the behavior at the root is characterized using sliding and separation intensity indicators, which are defined as

$$J_T = \frac{1}{K_c} \sum_{k=1}^{K_c} \left(\int_0^T \left| \dot{q}_{T_k}(t) \right| dt \right) \tag{17}$$

$$J_N = \frac{1}{K_c} \sum_{k=1}^{K_c} \left(\frac{1}{T} \int_0^T \mathrm{q}_{N_k}(t)\, dt \right) \tag{18}$$

In this manner, the parameters J_T and J_N represent the total amount of sliding and the average separation, respectively, that occur across the entire contact interface during one vibration cycle.

Figure 6 presents the normalized root-mean-square displacement amplitude at the blade tip and the associated blade root sliding and separation intensity indicators frequency response functions. These results reveal a classical friction damping behavior, analogous to that observed in blades equipped with dry friction dampers. An *optimal* coefficient of friction near $\mu \approx 0.4$ produces the greatest reduction in the peak tip response across the resonance bandwidth. Lower friction values shift the resonant frequency downward and increase displacement amplitudes, promoting free sliding. Conversely, higher friction values elevate the resonant frequency, stiffening the contact interface and nearing full-stick conditions, thereby producing larger peak displacements. These trends are clearly reflected in the frequency responses of the sliding and separation indicators: peak sliding diminishes with increasing friction, while separation exhibits a conventionally damped response, effectively suppressing lift-off effects. The optimally damped response is hence that with the greatest amount of slip accommodation that does not promote excessively detached (frictionless) sliding in the contact interface.

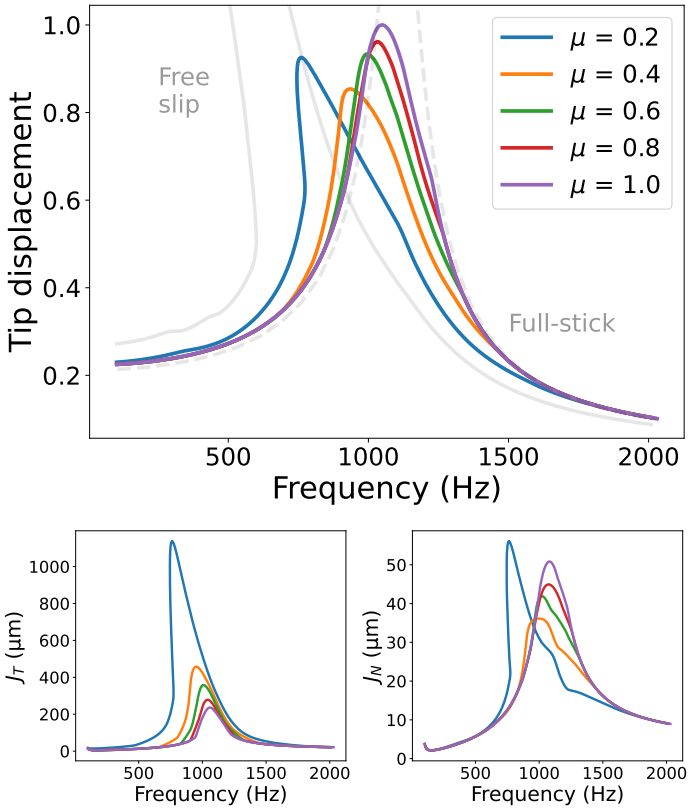

FIGURE 6. Normalized blade tip displacement amplitude (top), sliding intensity (J_T) (left), and separation intensity (J_N) (right) frequency response functions

FRETTING WEAR

In this section, the relationship between surface wear and the stick-slip motion is examined, together with its influence on blade tip displacements. Herein, the dynamic response and wear patterns are obtained over 3000 vibration cycles. Wear is computed on the blade root interface at the conclusion of each contact cycle according to Equation 16 with a wear coefficient $k_w = 10^{-11}$. Fretting wear effects are characterized twofold: Firstly, for a range of coefficients of friction at a constant near-resonance frequency of 1000 Hz, and secondly, for a constant coefficient of friction $\mu = 0.2$ for sub- near- and

super-resonance conditions between 500 and 1500 Hz.

The change in geometry of the contact interface over repeated loading cycles is shown in Figure 7, illustrating the evolution of a top contact interface under near-resonance, low-friction conditions together with the final wear patterns from higher-friction simulations. The repeated effect of material removal is reflected in the steadily decreasing wear depth of the colored surface. The surface also becomes increasingly curved, with greater wear localized toward the periphery of the contact zone. This behavior is attributed to the elevated normal loads that arise in these regions during the blade's oscillations, as was shown in Figure 5. Comparing the final wear patterns demonstrates that low-friction conditions promote higher amounts of surface wear. Moreover, these wear patterns are too more intensely worn at the peripherals. Collectively, these trends are attributed to the greater amounts of homogeneous sliding that occurs when there are lower amounts of frictional activity.

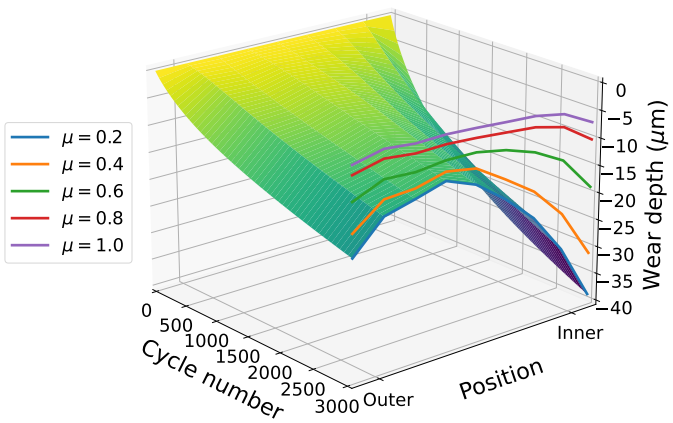

FIGURE 7. Wear-induced surface profile for $\mu = 0.2$ and final higher friction wear patterns of the top left blade root contact interface, at the near-resonance frequency of 1000 Hz

Equivalently, Figure 8 illustrates these effects across the entire root contact interface. The figure presents the wear patterns of all four contact interfaces (arranged physically as in Figure 3) for several vibration cycles. This comparison highlights wear disparities not only between the top and bottom surfaces, but also between adjacent ones. Differences in the form and intensity of wear between the top and bottom surfaces arise from the geometry of the contact problem. In particular, the top surfaces closer to the point of load application experience higher stresses and are consequently more worn. In contrast, differences between adjacent contact interfaces are less straightforward.These dissimilarities result from variations in the distribution of the normal contact forces. More specifically, they arise from the asymmetry in peak magnitudes at the periphery, as shown in Figure 5. These differences are attributed to frictional asymmetries in the root joint and the coupling between the blade tip and root; wherein nominally symmetric centrifugal and harmonic tip-excitation loads induce positionally biased deformations. In fact, the first mode shape depicted in Figure 2 closely resembles the mean position of the blade under symmetric loading. Inherently, these effects accentuate normal contact loads, thereby increasing wear severity in the left-most contact interfaces. In practice, this phenomenon persists when asymmetric loading dominates the response. This occurs in high-speed aeroengine applications or when large rigid-body displacements arise, which are synonymous with intermittent load cycles and substantial bladed-disk clearance distances.

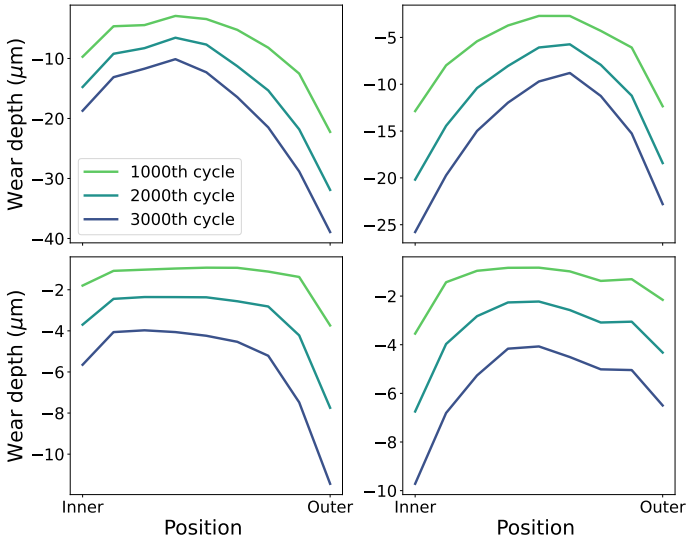

FIGURE 8. Wear pattern evolution on all blade root contact interfaces for $\mu = 0.2$ at the near-resonance frequency of 1000 Hz (organized physically as in Figure 3)

The effects of surface wear on the dynamics of the bladed disk structure are summarized in Figure 9. Herein, the evolution of the sliding indicator (left) and normalized tip displacements (right) with respect to wear are presented for a range of friction coefficients near-resonance (top). Furthermore, sub-, near-, and super-resonance results are further presented for low friction conditions (bottom). Overall, near-resonance sliding distances are generally observed to increase with wear in a manner that is

accentuated for higher coefficients of friction. To this end, the lowest coefficient, $\mu = 0.2$ exhibits a largely constant amount of sliding. This phenomenon is intriguing as it was observed earlier that reduced friction activity elevates wear magnitudes. Furthermore, the normalized tip displacements are observed to reduce with the progression of wear for lower coefficients of friction. This effect is, however, reduced for higher coefficients of friction and even reversed for the highest value of $\mu = 1$. These trends are attributed to the reduced influence of sliding at higher coefficients of friction where stick dominates the dynamic response.

Furthermore, the effects of surface wear at sub- and super-resonance differ markedly from those observed near resonance. In the off-resonance regimes, sliding and tip displacements are reduced across all wear magnitudes, as is classically expected. Notably, sliding remains largely constant over all vibration cycles, appearing independent of excitation frequency. These variations, though small in absolute terms, constitute a larger fraction of the off-resonance response. This behavior may be specific to low-friction conditions though, since more pronounced variations were observed for higher friction levels. For tip displacements, wear dependence is considerably stronger near resonance than in the off-resonance cases. This observation is intuitive, since larger wear magnitudes tend to coincide with higher response levels; by contrast, it is shown that sliding distances show a weaker sensitivity. Hence, this trend is likely associated with differences in root-interface contact forces.

CONCLUSION

This paper presents a compact Equality-based Weighted Residual (E-WR) frequency-domain framework for modeling fretting wear under oscillatory contact, incorporating both one-dimensional friction with separation and wear. Frictional contact is modeled through a non-smooth, equality-based formulation of the Signorini and Coulomb conditions. These conditions are then resolved alongside the governing equations of elasticity in a weak sense using a harmonic balance-based approach, to yield the periodic forced responses. Wear is introduced within a dual time scale formulation that computes the evolution of the gap function on which impenetrability is defined for a series of successive contact problems.

The new methodology has been applied to the study of a simplified yet representative bladed disk model subject to harmonic blade tip excitation. The E-WR method was first validated in the absence of wear. Then, extended studies into the coupled effects of friction and wear were performed across a range of excitation frequencies. These results focused on the dynamic response at the blade root and tip. Without wear, classical frictional-dampening effects were recovered with an optimally subdued peak response corresponding to a friction coefficient of $\mu \approx 0.4$. At higher friction levels, the response approaches the free-stick limit, whereas at lower values it tends toward frictionless sliding.

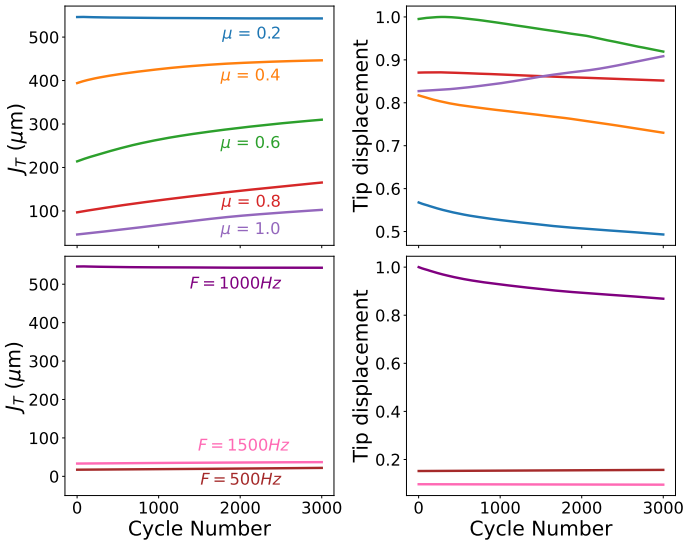

FIGURE 9. Friction-wear dependence at the near-resonance frequency of 1000 Hz (top) and frequency-wear dependence for $\mu = 0.2$ (bottom) of sliding distance (left) and blade tip displacement amplitude (right)

Wear magnitudes were greater for lower coefficients of friction as larger sliding distances arose. The peripherals of the contact interface were also more severely worn due to increased normal contact forces in these external regions. Near resonance conditions, wear had a diminishing effect of reducing sliding distances for lower coefficients of friction. Conversely, the effect on tip displacements was non-monotonic. In this manner, lower coefficients of friction reduced peak displacements while higher coefficients increased them. At off-resonance excitation frequencies, wear was observed to reduce sliding and tip displacements. In comparison, near resonance, the tip response was more wear-dependent in a manner that is closely linked to root-interface contact forces. Overall, these results demonstrate the complex interplay between stick-slip, separation and wear in a bladed disk structure across a range of aeroelastic vibration frequencies.

ACKNOWLEDGMENTS

This project was supported by funds from the GUIde Consortium at Duke University. The findings, opinions, and recommendations expressed herein are those of the author(s) and are not necessarily those of Duke University or the GUIde Consortium Members.

Safran Helicopter Engines company is gratefully acknowledged for providing the model. In this paper, there is no data representative of an actual Safran Helicopter Engines wheel.

REFERENCES

[1] Peter Wriggers and Tod A Laursen. *Computational contact mechanics*, volume 2. Springer, 2006.

[2] Vincent Acary. Energy conservation and dissipation properties of time-integration methods for nonsmooth elastodynamics with contact. *ZAMM-Journal of Applied Mathematics and Mechanics*, 96, 2016.

[3] Samuel Nacivet, Christophe Pierre, Fabrice Thouverez, and Louis Jézéquel. A dynamic Lagrangian frequency–time method for the vibration of dry-friction-damped systems. *Journal of Sound and Vibration*, 2003.

[4] J. F. Archard. Contact and rubbing of flat surfaces. *Journal of Applied Physics*, 24:981–988, 1953.

[5] Loïc Salles, Laurent Blanc, Fabrice Thouverez, Aleksander M Gouskov, and Pierrick Jean. Dynamic analysis of a bladed disk with friction and fretting-wear in blade attachments. In *Turbo Expo: Power for Land, Sea, and Air*, volume 48876, 2009.

[6] E Lemoine, D Nélias, F Thouverez, and C Vincent. Influence of fretting wear on bladed disks dynamic analysis. *Tribology International*, 145, 2020.

[7] Mathias Legrand and Christophe Pierre. A compact, equality-based weighted residual formulation for periodic solutions of systems undergoing frictional occurrences. *Journal of Structural Dynamics*, 2024.

[8] Vincent Acary and Bernard Brogliato. *Numerical methods for nonsmooth dynamical systems: applications in mechanics and electronics*. Springer Science & Business Media, 2008.

[9] Arash Hashemi, Christophe Pierre, and Mathias Legrand. An equality-based weighted residual formulation for the vibration of systems with two-dimensional friction. *Journal of Structural Dynamics*, 3:127–155, 08 2025.

[10] Erhan Ferhatoglu, Johann Groß, and Malte Krack. Frequency response variability in friction-damped structures due to non-unique residual tractions: Obtaining conservative bounds using a nonlinear-mode-based approach. *Mechanical Systems and Signal Processing*, 201:110651, 2023.

[11] Georges Verchery. Régularisation du système de l'équilibre des structures élastiques discrètes. *Comptes rendus de l'Académie des sciences. Série 2, Mécanique, Physique, Chimie, Sciences de l'univers, Sciences de la Terre*, 311, 1990.